

Piezovally effect and magnetovally coupling in altermagnetic semiconductors

Weifeng Xie¹, Xiong Xu², Yunliang Yue³, Huayan Xia¹, Hui Wang^{2*}

¹School of Microelectronics and Physics, Hunan University of Technology and Business, Changsha 410205, China

²School of Physics, Hunan Key Laboratory of Super Microstructure and Ultrafast Process, Hunan Key Laboratory of Nanophotonics and Devices, State Key Laboratory of Powder Metallurgy, Central South University, Changsha 410083, China

³College of Information Engineering, Yangzhou University, Yangzhou 225127, China

Abstract

Clarifying the physical origin of valley polarization and exploring new ferrovalley materials are conducive to the application of valley degrees of freedom in the field of information storage. Here, we explore two new-type altermagnetic semiconductors (monolayers $\text{Nb}_2\text{Se}_2\text{O}$ and Nb_2SeTeO) with above-room-temperature Néel temperature based on first-principles calculations. It reveals that uniaxial strain induces valley polarization without spin-orbital coupling (SOC) in altermagnets owing to the piezovally effect, while uniaxial compressive strain transforms from ferrovalley semiconductor to semimetal, half metal and metal. Moreover, moderate biaxial strain renders Janus monolayer Nb_2SeTeO to robust Dirac-like band dispersion. The SOC and intrinsic in-plane magnetocrystalline anisotropy energy induces Dirac-like altermagnets to generate apparent valley polarization through magnetovally coupling. In terms of SOC perturbation, we elucidate the physical mechanism behind in-plane-magnetization induced valley polarization and point out the magnitude of valley polarization is positively correlated with the square of SOC strength and negatively correlated with the bandgap. The present work reveals the physical origin of valley polarization in altermagnets and expands the application of ferrovalley at room temperature in valleytronics.

Introduction

Valley, a new degree of freedom, characterized by two inequivalent but energy-degenerate valley points near Fermi level on band structures, which can be used as information coding, manipulation and transportation in valleytronics¹⁻³. The early studies of valley degree of freedom as a potential information carrier was proposed in AAs two-dimensional (2D) electron system⁴. Then, graphene as a 2D prototype becomes a candidate due to its unequal two valley points (K and K') in hexagonal crystal structures^{3,5-7}. However, graphene has spatial inversion symmetry, gapless band structure and weak spin-orbital coupling (SOC) strength, hindering its application in practical electronic devices. After that, transition metal dichalcogenides (e.g. MoS₂, WSe₂) inspire extensive interests on the basis of priority of broken spatial inversion symmetry, controllable bandgap and considerable SOC effect⁸⁻¹¹. However, the degeneracy between two valleys needs to be lifted when manipulating the valley degree of freedom. In practice, extrinsic methods such as magnetic field¹²⁻¹⁵, magnetic doping^{16,17}, proximity effect¹⁸⁻²¹ and optical pumping with circularly polarized light^{9,22,23} have been implemented to lift the degenerate valley, while they are unbeneficial to control in valleytronics.

Recently, valley materials combining with ferromagnetism dubbed as ferrovalley have attracted great interests because ferrovalley not only breaks spatial inversion symmetry but also time-reversal symmetry². Generally, SOC with out-of-plane magnetization (M_{\perp}) induces valley polarization and anomalous valley Hall effect can be generated under proper carriers doping and in-plane electric field^{2,24-27}. So far, most 2D ferrovalley materials are demonstrated as small valley polarization and perpendicular magnetocrystalline anisotropy energy (MAE), low Curie temperature or in-plane MAE which cannot spontaneously induce valley polarization^{2,28-32}. Moreover, most of the investigated 2D ferrovalley materials belong to ferromagnetic (FM) or antiferromagnetic (AFM) systems in which three indispensable conditions result in spontaneous valley polarization: (i) magnetic exchange interaction, (ii) SOC interaction and (iii) perpendicular MAE. Therefore, breaking these prerequisites and exploring novel physical mechanisms of generating valley polarization is imperative.

Recent discovery of altermagnetic (AM) materials³³⁻³⁷ conjugate the characteristic of ferromagnetism and antiferromagnetism, and the degeneracy of opposite spin states is lifted as ferromagnets but keeping zero net magnetic moment as antiferromagnet, making them very promising for valley polarization application. It has been reported that valley polarization can be induced by piezovalley in 2D altermagnets³⁸⁻⁴², the value of valley polarization without considering SOC is apparently larger than that with SOC and the value is tunable with different uniaxial strain. On the other hand, generally, perpendicular MAE stabilizes long-range magnetic order of 2D systems at finite temperature⁴³, in which valley polarization can be generated under the action of SOC². Otherwise, external out-of-plane magnetic field is needed to transfer the direction of magnetization to out of plane⁴⁴⁻⁴⁶. However, many 2D magnetic materials intrinsically possess isotropic in-plane MAE, it is important to explore whether in-plane magnetization (M_{\parallel}) can spontaneously induce valley polarization.

In this work, we explore two new-type 2D AM monolayers Nb₂Se₂O and Nb₂SeTeO via first-principles calculations. It is found that both of them can be induced a large valley polarization under a moderate uniaxial strain without SOC, ascribed mainly to the piezovally coupling effect. Moreover, the properties of altermagnets can be transformed under different uniaxial strain. Furthermore, appropriate biaxial compressive strain transforms Nb₂SeTeO from Janus semiconductors to robust Dirac-like semimetals. M_{\parallel} induces Nb₂SeTeO to generate valley polarization when SOC is considered, and the physical mechanisms behind the magnetovally coupling are elucidated in terms of SOC perturbation theory.

Methods

First-principles calculations based on density functional theory are performed via projected augmented-wave method⁴⁷ implemented in Vienna *ab-initio* simulation package (VASP)⁴⁸. The exchange-correlation function is treated by the Perdew-Burke-Ernzerhof parameterization of the generalized gradient approximation⁴⁹. The energy cutoff of the plane-wave basis is set as 600 eV. $U = 4$ eV is adopted to describe the strongly localized d orbitals of the Nb atom. In Fig. S1 in the **Supplemental Materials**, we have confirmed the reasonability of $U = 4$ eV through comparing the band gap between PBE + U and HSE06. A Monkhorst-Pack grid is chosen to be $13 \times 13 \times 1$ for the structural relaxation and self-consistent calculation. The convergent threshold of energy is set as 1×10^{-7} eV and that of the force is less than 0.001 eV \AA^{-1} . Based on the force theorem^{50,51}, the distribution of MAE is calculated in VASP by directly obtaining the energy difference between different direction of magnetization and z [001] directions when SOC is considered, which can be written as $\text{MAE} = E_{\theta,\varphi} - E_{[001]}$, where θ and φ represents polar angle and azimuthal angle of the magnetization, respectively. The PHONOPY code⁵² based on the finite displacement method is adopted to obtain the phonon dispersion spectrum by using a $5 \times 5 \times 1$ supercell including 125 atoms. The *ab initio* molecular dynamics (AIMD) simulations⁵³ are carried out using $5 \times 5 \times 1$ supercell at 300 K with a 1 fs time step. Monte Carlo simulations with the Heisenberg model are performed in VAMPIRE^{54,55} to estimate Néel temperature.

Results and Discussion

The Hamiltonian of valley polarization can be written in term of magnetic exchange coupling and SOC interaction², $\mathcal{H}(\mathbf{k}) = \mathcal{H}_0(\mathbf{k}) + \mathcal{H}_{ex}(\mathbf{k}) + \mathcal{H}_{SOC}(\mathbf{k})$. In transition metal dichalcogenides, the valley-related properties take place in the vicinity of valleys of the lowermost conduction band (LCB) or uppermost valence band (UVB) that primarily consists of the hybridization of d_{xy} and $d_{x^2-y^2}$ orbitals of the transition metal⁵⁶. When M_{\perp} is imposed, the valley polarization emerges, as schematically illustrated in Fig. 1 (a) and (b). It is noticed that such valley polarization is normally found in FM or AFM materials. Recent altermagnets have been received extensive attention^{33,34}, it is reported that the valley polarization can be reversibly

induced by moderate uniaxial strain due to the piezovally coupling^{38–40} as shown in Fig. 1 (c) and (d). Interestingly, we introduce a distinct physical mechanism of the generation of valley polarization, namely, M_{\parallel} induces the valley polarization in Dirac-like altermagnets when SOC is considered, the schematic illustration is shown in Fig. 1 (e) and (f).

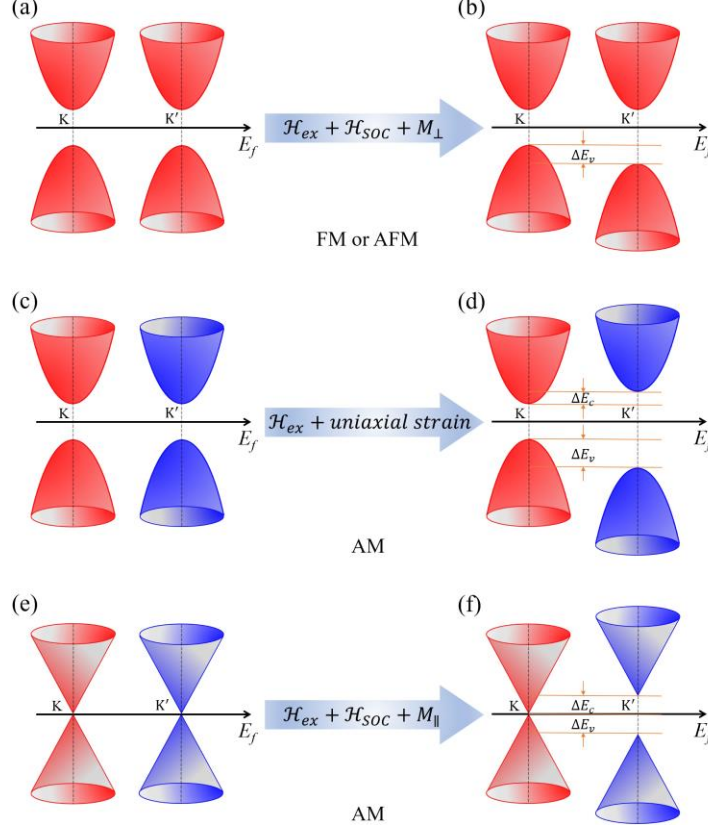


Fig. 1. Schematic illustration of valley polarization induced by (a) and (b) magnetic exchange interaction (\mathcal{H}_{ex}), SOC interaction (\mathcal{H}_{SOC}) and out-of-plane magnetization (M_{\perp}), (c) and (d) \mathcal{H}_{ex} and uniaxial strain, (e) and (f) \mathcal{H}_{ex} , \mathcal{H}_{SOC} and in-plane magnetization (M_{\parallel}), where red and blue represent spin-up and spin-down bands, respectively, and ΔE_v and ΔE_c represent valley polarization of uppermost valence band and lowermost conduction band, respectively. E_f is Fermi level.

In Fig. 2 (a) and (b), we show the top and side views of $\text{Nb}_2\text{Se}_2\text{O}$ and Nb_2SeTeO monolayers, respectively. Their ground-state geometrical structures have a $P4/mmm$ space group, the inversion symmetry of Nb_2SeTeO is broken due to the Janus structure. Both of them have a mirror symmetry along diagonal direction shown in Fig. 2 (a) and (b). Phonon spectrum and AIMD simulation are adopted to verify the kinetic and thermodynamic stabilities, respectively, as demonstrated by the non-apparent imaginary frequencies in Fig. 2 (c-d) and non-apparent energy fluctuations and structural deformations at 300 K in Fig. 2 (e-f).

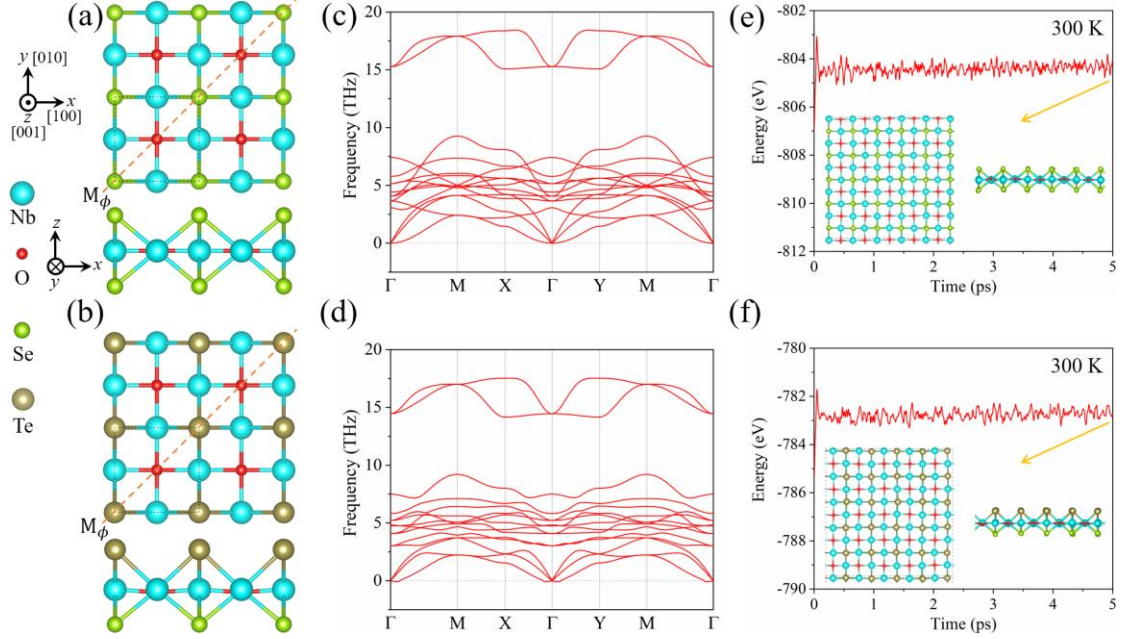


Fig. 2. Structures and stability. (a) and (b) Top and side views, (c) and (d) phonon spectrums, (e) and (f) AIMD simulations at 300 K for monolayers $\text{Nb}_2\text{Se}_2\text{O}$ and Nb_2SeTeO , respectively. In (a) and (b), the black dotted line box represents the unit cell, the orange dotted line (M_ϕ) denotes diagonal mirror symmetry in xy plane. Insets in (c) and (f) are the snapshots after 5 ps at 300 K.

Through comparison of different magnetic state, we find that AFM state is 388.108 meV (339.913 meV) lower than FM state for $\text{Nb}_2\text{Se}_2\text{O}$ (Nb_2SeTeO). We plot the spin densities of $\text{Nb}_2\text{Se}_2\text{O}$ and Nb_2SeTeO , as shown in Fig. 3 (a) and (b), respectively. The spin density of $\text{Nb}_2\text{Se}_2\text{O}$ and Nb_2SeTeO cannot be operated through inversion or translation symmetry, the rotational operation is needed instead, which is the characteristic of altermagnets^{33,34}. The band structures with non-degenerate opposite spins (Fig. 4 (a) and (e)) also demonstrate that $\text{Nb}_2\text{Se}_2\text{O}$ and Nb_2SeTeO are altermagnets. In magnetic materials, through defining MAE as the energy difference between hard and easy magnetic axis, we find that $\text{Nb}_2\text{Se}_2\text{O}$ and Nb_2SeTeO both have in-plane MAE with a value of 0.632 meV and 0.697 meV, respectively, as shown in Fig. 3 (c) and (d). The first nearest-neighbor J_1 , next nearest-neighbor J_2 , third nearest-neighbor J_3 and fourth nearest-neighbor J_4 magnetic exchange interaction (defined in Fig. 4 (a) and (b)) are calculated in TB2J software package⁵⁷ based on the Heisenberg model described as follows:

$$\mathcal{H} = -\sum_{i \neq j} J_{ij} \mathbf{S}_i \cdot \mathbf{S}_j - A \sum_i (S_i^z)^2, \quad (1)$$

where J_{ij} represents the exchange strength between the magnetic atoms at i and j sites, \mathbf{S} is a unit vector which describes the orientation of the spin of magnetic atom, the superscript z represent the z component of the spin, and A is the value of MAE. According to Eq. (1), the calculated values of J_1 , J_2 , J_3 and J_4 are shown in Fig. 3 (e) and (f). In $\text{Nb}_2\text{Se}_2\text{O}$, J_1 is negative with a value of ~ 30 meV, which means the first nearest-neighbor exchange of magnetic atoms are inclined to antiparallel arrangement. Intriguingly, J_2 has two different indirect exchange paths, one is Nb-Se-Nb

superexchange interaction J_2^{Se} and the other is Nb-O-Nb superexchange interaction J_2^O . The calculated results show that J_2^{Se} and J_2^O are positive, indicating the FM coupling. Moreover, J_2^{Se} is smaller than J_2^O , meaning the superexchange exchange strengths between Nb-Se-Nb and Nb-O-Nb are inequivalent. Similarly, for Janus Nb₂SeTeO, there are slight difference between two next nearest-neighbor exchange interaction $J_2^{Se/Te}$ and J_2^O , the positive value also indicates the FM coupling between them. The estimated Néel temperatures of Nb₂Se₂O and Nb₂SeTeO are 835 K and 745 K, respectively, promising for application near room temperature.

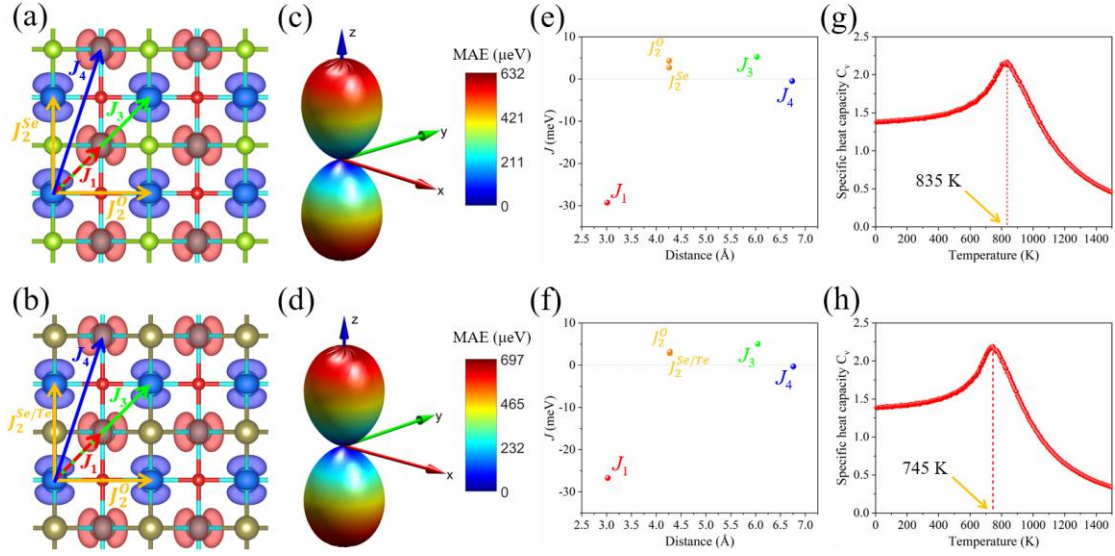


Fig. 3. (a) and (b) Spin densities, (c) and (d) three-dimensional distribution of MAE, (e) and (f) values of magnetic exchange interaction, (g) and (h) specific heat capacity as a function of temperature for monolayers Nb₂Se₂O and Nb₂SeTeO, respectively. In (a) and (b), the isosurface is plotted at $2 \times 10^{-2} e/Bohr^3$ with the red and blue colors representing the positive and negative values, respectively, and the nearest-neighbor J_1 , next nearest-neighbor J_2 , third nearest-neighbor J_3 and fourth nearest-neighbor J_4 magnetic exchange interaction are labeled.

Strain engineering is an effective way to regulate the physical properties as well as generate novel physical phenomena. The intrinsic band structures of Nb₂Se₂O and Nb₂SeTeO are shown in Fig. 4 (a) and (e). Differing from the antiferromagnets, the splitting of opposite spins in reciprocal space confirms the feature of altermagnets. It is shown that the bandgaps of Nb₂Se₂O and Nb₂SeTeO are 336.382 meV and 84.226 meV, respectively, which manifests them as AM semiconductors. As shown in Fig. 4 (b)-(d), we find that uniaxial strain induces valley polarization in Nb₂Se₂O and effectively regulate the magnitude and sign of valley polarization even without SOC. Under strain of -3.44%, valley polarization reach maximum value of 264.076 meV at UVB, which is significantly larger than that induced by SOC^{2,27,30,58-61}. Interestingly, we also find that uniaxial strain along x/y direction can precisely regulate the bandgap of valleys at X/Y point, transforming Nb₂Se₂O from ferrovalley semiconductor (FVS) to semimetals at a critical compressive strain of -3.44%, as shown in Fig. 4 (b) and (c). Differently, the tensile strain does not change the property of material but can linearly

increase the magnitude of valley polarization, as shown in Fig. 4 (d). The regulation of uniaxial strain on valley polarization of Nb₂SeTeO is mostly akin to the phenomena in Nb₂Se₂O and can reverse the sign of valley polarization as shown in Fig. 4 (f) and (g). In Fig. 4 (h), one may note that under compressive strain Nb₂SeTeO transforms from FVS to semimetal at critical -1.71% and at the interval of compressive strain varying from -1.71% to -2.20%, half metal property is presented.

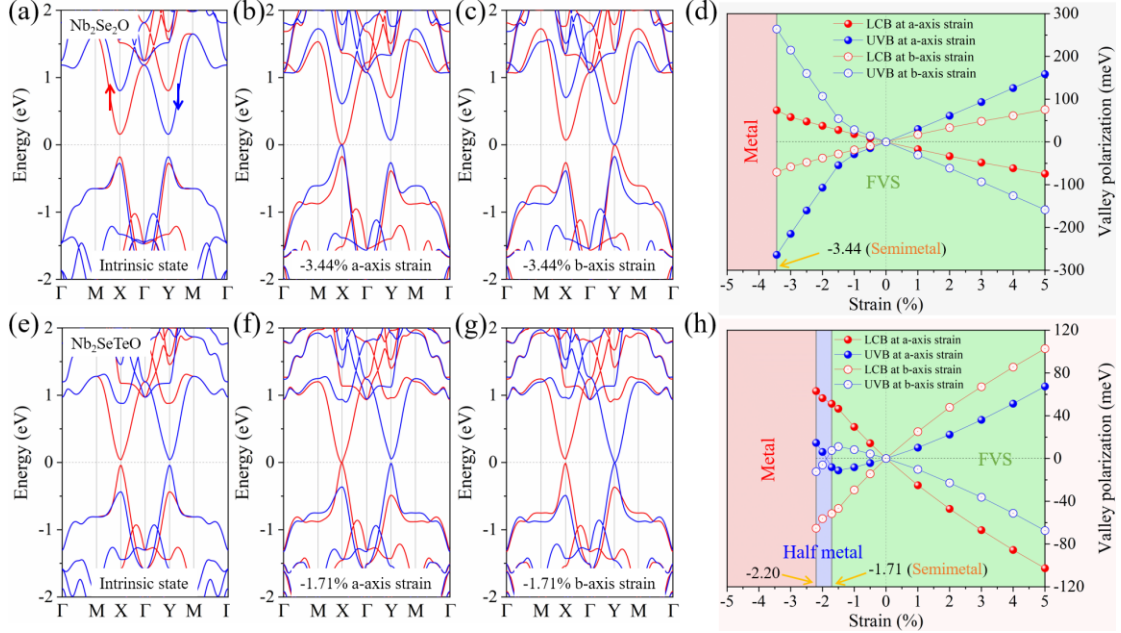


Fig. 4. Band structures without SOC at (a) intrinsic state, (b) -3.44% x -axis and (c) -3.44% y -axis compressive strains, (d) valley polarization and properties versus uniaxial strain for monolayer Nb₂Se₂O. (e)-(h) The same as (a)-(d) but for monolayer Nb₂SeTeO, and (f) and (g) correspond to band structures at -1.77% x -axis and -1.77% y -axis compressive strains, respectively. The red and blue lines represent the spin-up and spin-down bands, respectively. The Fermi level is set as zero on the band structures.

As a further step, biaxial strain is considered as well to adjust and control the electronic structure. As shown in Fig. 5 (a), it is found that the bandgap of Janus Nb₂SeTeO gradually decreases under biaxial compressive strain, and almost closed at a larger compressive strain displaying Dirac-like band dispersion (as shown in Fig. S2 (a)-(e) in the **Supplemental Materials**). One should note that the Dirac-like band is robust under biaxial compressive strain up to -5%, the 3D band structure is shown in Fig. 5 (b). Taking biaxial compressive strain of -4% as an example, we consider the effect of SOC on band structure, as demonstrated in Fig. 6. Surprisingly, we found that M_{\parallel} [100] direction induces an apparent valley polarization that is reversible as magnetization turns to [010] direction. However, M_{\perp} [001] cannot induce valley polarization, as shown in Fig. S3 in **Supplemental Materials**.

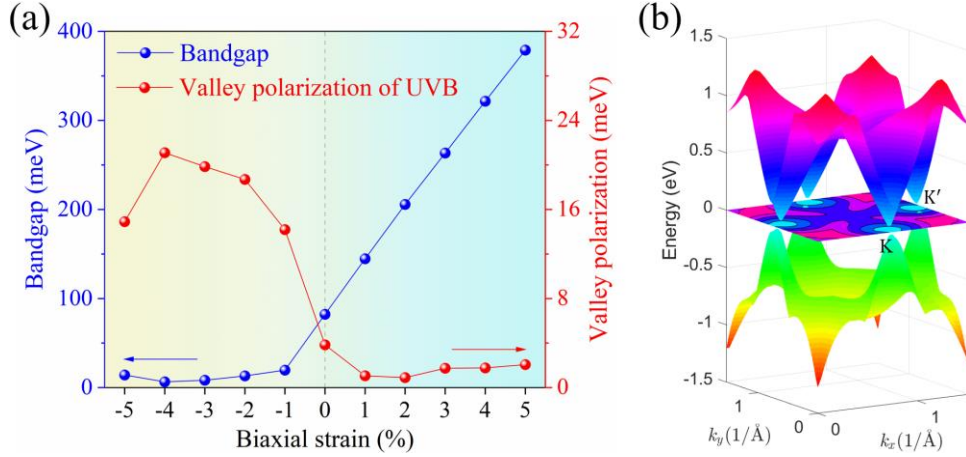


Fig. 5. (a) Variation of bandgap and valley polarization of UVB induced by SOC with [100] magnetization as a function of biaxial strain in monolayer Nb₂SeTeO. (b) Three-dimensional band structures of Nb₂SeTeO at -5% biaxial compressive strain, where Fermi level is set as zero.

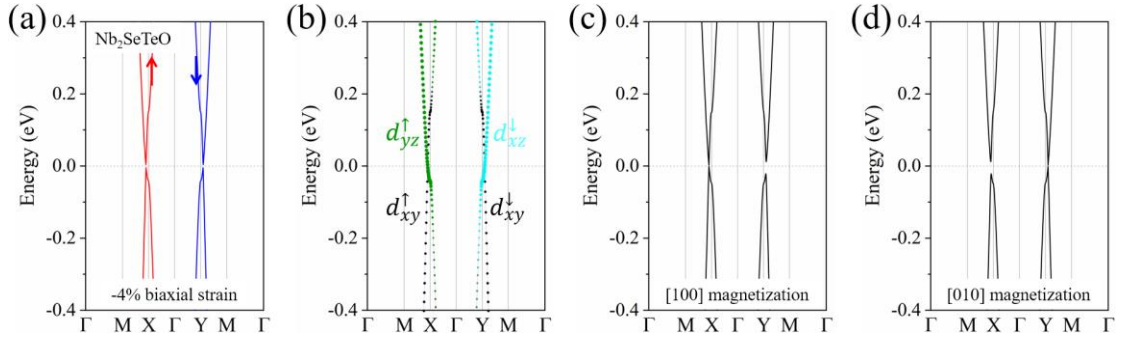


Fig. 6. For Nb₂SeTeO at -4% biaxial compressive strain. (a) Band structure and (b) d -orbitals-resolved band structure without considering SOC. Band structures under SOC with (c) [100] magnetization and (d) [010] magnetization. The Fermi level is set as zero on the band structures.

From Fig. 6 (a), we define two valleys near the X and Y high-symmetry points as K and K', respectively. It is found that the bands at K and K' are contributed by spin-up and spin-down bands, respectively. Therefore, we only consider the spin-conserving SOC Hamiltonian from the same spin channels which can be written as:

$$\hat{\mathcal{H}}_{SOC} = \lambda \hat{S}_{z'} \left(\hat{L}_z \cos\theta + \frac{1}{2} \hat{L}_+ e^{-i\varphi} \sin\theta + \frac{1}{2} \hat{L}_- e^{i\varphi} \sin\theta \right), \quad (2)$$

where λ represents the SOC coefficient, $\hat{S}_{z'}$ and \hat{L}_z represent the z' or z components of spin and orbital angular momentum, respectively, θ and φ are the polar angle and azimuthal angle of the spin, respectively, and the ladder operators are given by $\hat{L}_+ = \hat{L}_x + i\hat{L}_y$, $\hat{L}_- = \hat{L}_x - i\hat{L}_y$. The orbitals-resolved band structures in Fig. 6 (b) show that

d_{xy}^\uparrow and d_{yz}^\uparrow orbitals of Nb have a dominant contribution at K valley near the Fermi

level, while bands at K' valley are mainly contributed by d_{xy}^\downarrow and d_{xz}^\downarrow orbitals.

According to the representation of the d -orbital spherical harmonic function $d_{xy} =$

$-\frac{i}{\sqrt{2}}(Y_2^2 - Y_2^{-2})$, $d_{yz} = \frac{i}{\sqrt{2}}(Y_2^1 + Y_2^{-1})$ and $d_{xz} = -\frac{1}{\sqrt{2}}(Y_2^1 - Y_2^{-1})$, the matrix of

SOC coupling between different d orbitals can be constructed. For K valley, the coupling matrix representation between d_{xy}^\uparrow and d_{yz}^\uparrow through the spin-conserving SOC Hamiltonian (Eq. (2)) can be written as:

$$[\mathcal{H}^{(K)}] = [\mathcal{H}_0] + [\mathcal{H}_{SOC}^{(K)}] = \begin{bmatrix} \varepsilon_1 & i\alpha \sin\theta \sin\varphi \\ -i\alpha \sin\theta \sin\varphi & \varepsilon_2 \end{bmatrix}, \quad (3)$$

where $\alpha = \lambda \hat{S}_z'$, ε_1 and ε_2 represent the energy levels of valence band maximum (VBM) and conduction band minimum (CBM), respectively, without SOC perturbation. Through diagonalizing the matrix in Eq. (3), the eigenvalues ($\varepsilon_{\pm}^{(K)}$) corresponding to the energy levels of VBM and CBM at K valley after perturbation

are obtained as $\varepsilon_{\pm}^{(K)} = \frac{\varepsilon_1 + \varepsilon_2 \pm \sqrt{\Delta_0^2 + 4\alpha^2 \sin^2\theta \sin^2\varphi}}{2}$, where $\Delta_0 = \varepsilon_1 - \varepsilon_2$ represents the bandgap without SOC perturbation. Therefore, the changed bandgap at K valley ($\Delta^{(K)}$) after SOC perturbation can be represented as

$$\Delta^{(K)} = \varepsilon_+^{(K)} - \varepsilon_-^{(K)} = \sqrt{\Delta_0^2 + 4\alpha^2 \sin^2\theta \sin^2\varphi}. \quad (4)$$

For K' valley, the coupling matrix representation between d_{xy}^\downarrow and d_{xz}^\downarrow through the spin-conserving SOC Hamiltonian (Eq. (2)) can be written as:

$$[\mathcal{H}^{(K')}] = [\mathcal{H}_0] + [\mathcal{H}_{SOC}^{(K')}] = \begin{bmatrix} \varepsilon_1 & -i\alpha \sin\theta \cos\varphi \\ i\alpha \sin\theta \cos\varphi & \varepsilon_2 \end{bmatrix}, \quad (5)$$

Through diagonalizing the matrix in Eq. (5), the eigenvalues $\varepsilon_{\pm}^{(K')}$ corresponding to VBM and CBM at K' valley after perturbation are obtained as $\varepsilon_{\pm}^{(K')} =$

$\frac{\varepsilon_1 + \varepsilon_2 \pm \sqrt{\Delta_0^2 + 4\alpha^2 \sin^2\theta \cos^2\varphi}}{2}$. The changed bandgap at K' valley ($\Delta^{(K')}$) after SOC perturbation can be represented as

$$\Delta^{(K')} = \varepsilon_+' - \varepsilon_-' = \sqrt{\Delta_0^2 + 4\alpha^2 \sin^2\theta \cos^2\varphi}. \quad (6)$$

As shown in Fig. 6 (a), under -4% biaxial compressive strain, Nb₂SeTeO monolayer presents Dirac-like band dispersion. It is reasonable that we approximatively treat $\varepsilon_1 = \varepsilon_2 \approx 0$, that is $\Delta_0 = 0$. So, Eq. (4) and Eq. (6) can be simplified as

$$\begin{cases} \Delta^{(K)} = 2\alpha \sin\theta \sin\varphi, & \text{at K valley} \\ \Delta^{(K')} = 2\alpha \sin\theta \cos\varphi, & \text{at K' valley} \end{cases} \quad (7)$$

When the magnetization is along [100] direction, that is $\theta = 90^\circ$, $\varphi = 0^\circ$, According to Eq. (7), we can deduce that the bandgap after SOC perturbation at K valley remains basically unchanged, namely, the bandgap is equal to zero. However, the SOC

perturbation opens the bandgap at K' valley whose value is equal to 2α . The inequivalent bandgaps at K and K' valleys induced by SOC is the main reason of the generation of valley polarization, the results are consistent with Fig. 6 (c). Similarly, when the magnetization turns to $[010]$ direction, that is $\theta = 90^\circ$, $\varphi = 90^\circ$, the bandgap at K valley is opened and its value is equal to 2α , the bandgap at K' valley remains almost zero, consistent with first-principles calculations. From Eq. (7), we also can conclude that the case of $\theta = 90^\circ$ and $\varphi = 0^\circ$ or 90° can render the valley polarization to reach maximum value 21.10 meV and the signs of valley polarization at $\varphi = 0^\circ$ and $\varphi = 90^\circ$ are opposite. The phenomenon is akin to valley polarization induced by the M_\perp in which opposite M_\perp can reverse the sign of valley polarization.

The above discussed case is $\varepsilon_1 = \varepsilon_2 \approx 0$. If $\varepsilon_1 \neq 0$ and $\varepsilon_2 \neq 0$, according to Maclaurin formula, Eq. (4) and Eq. (6) can be expressed as:

$$\begin{cases} \Delta^{(K)} \approx \Delta_0 + \frac{2\alpha^2 \sin^2 \theta \sin^2 \varphi}{\Delta_0}, & \text{at K valley} \\ \Delta^{(K')} \approx \Delta_0 + \frac{2\alpha^2 \sin^2 \theta \cos^2 \varphi}{\Delta_0}, & \text{at K' valley} \end{cases}. \quad (8)$$

As shown Fig. S2 in **Supplemental Materials**, considering the approximate electron-hole symmetry on strain-tunable band structures of Janus Nb_2SeTeO monolayer, the valley polarization (ΔE) for $[100]$ and $[010]$ magnetization can be deduced as

$$\Delta E \approx \pm \frac{\alpha^2}{\Delta_0}. \quad (9)$$

Apparently, the magnitude of valley polarization is positively correlated with α^2 and negatively correlated with Δ_0 on the basis of Eq. (9). Fig. 5 (a) shows that biaxial compressive strain can lower the bandgap of Nb_2SeTeO . Thus, under the consideration of SOC with $[100]$ magnetization, the valley polarization gradually become larger. The deduced Eq. (9) is in line with the results of first-principles calculations and explain why we cannot observe apparent SOC-induced valley polarization when the bandgap is too large, as shown in Fig. S4 in **Supplemental Materials**. Moreover, Eq. (9) manifests that a large valley polarization is more incline to emerge in strong SOC systems. Therefore, we speculate the larger valley polarization induced by M_\parallel can be found in tetragonal altermagnets with strong SOC and small bandgap.

Conclusion

Through the first-principles calculations, we found that the valley polarization can be induced by uniaxial strain without considering SOC in AM semiconductors $\text{Nb}_2\text{Se}_2\text{O}$ and Nb_2SeTeO , both of which have in-plane magnetic easy axis and Néel temperature above room temperature. Uniaxial strains transform altermagnets between states of FVS, semimetal, half metal and metal. Biaxial strains render Janus Nb_2SeTeO to Dirac-like band dispersion, and SOC with M_\parallel generate sizeble valley polarization. The present work points out that valley polarization is positively correlated with the square of SOC strength and negatively correlated with the bandgap, providing guidance for valleytronic application.

Acknowledgement

This work was supported by National Natural Science Foundation of China (12174450, 11874429), National Talents Program of China, Science and Technology Innovation Program of Hunan Province (2024RC1013), Key Project of Natural Science Foundation of Hunan Province (Grant No. 2024JJ3029), Key Research and Development Program of Hunan Province (Grant No. 2022WK2002), Distinguished Youth Foundation of Natural Science Foundation of Hunan Province (2020JJ2039), Project of High-Level Talents Accumulation of Hunan Province (2018RS3021), Program of Hundreds of Talents of Hunan Province, State Key Laboratory of Powder Metallurgy, Start-up Funding and Innovation-Driven Plan (2019CX023) of Central South University, Postgraduate Scientific Research Innovation Project of Hunan Province (CX20230104, CX20220252). Calculations were performed at High-Performance Computing facilities of Central South University.

Reference

- (1) Schaibley, J. R.; Yu, H.; Clark, G.; Rivera, P.; Ross, J. S.; Seyler, K. L.; Yao, W.; Xu, X. Valleytronics in 2D Materials. *Nat Rev Mater* **2016**, *1* (11), 16055.
- (2) Tong, W.-Y.; Gong, S.-J.; Wan, X.; Duan, C.-G. Concepts of Ferrovalley Material and Anomalous Valley Hall Effect. *Nat Commun* **2016**, *7* (1), 13612.
- (3) Xiao, D.; Yao, W.; Niu, Q. Valley-Contrasting Physics in Graphene: Magnetic Moment and Topological Transport. *Phys. Rev. Lett.* **2007**, *99* (23), 236809.
- (4) Gunawan, O.; Shkolnikov, Y. P.; Vakili, K.; Gokmen, T.; De Poortere, E. P.; Shayegan, M. Valley Susceptibility of an Interacting Two-Dimensional Electron System. *Phys. Rev. Lett.* **2006**, *97* (18), 186404.
- (5) Rycerz, A.; Tworzydło, J.; Beenakker, C. W. J. Valley Filter and Valley Valve in Graphene. *Nature Phys* **2007**, *3* (3), 172–175.
- (6) Yao, W.; Xiao, D.; Niu, Q. Valley-Dependent Optoelectronics from Inversion Symmetry Breaking. *Phys. Rev. B* **2008**.
- (7) Zhang, F.; Jung, J.; Fiete, G. A.; Niu, Q.; MacDonald, A. H. Spontaneous Quantum Hall States in Chirally Stacked Few-Layer Graphene Systems. *Phys. Rev. Lett.* **2011**, *106* (15), 156801.
- (8) Xiao, D.; Liu, G.-B.; Feng, W.; Xu, X.; Yao, W. Coupled Spin and Valley Physics in Monolayers of MoS₂ and Other Group-VI Dichalcogenides. *Phys. Rev. Lett.* **2012**, *108* (19), 196802.
- (9) Mak, K. F.; McGill, K. L.; Park, J.; McEuen, P. L. The Valley Hall Effect in MoS₂ Transistors. *Science* **2014**, *344* (6191), 1489–1492.
- (10) Tao, L. L.; Tsymbal, E. Y. Two-Dimensional Spin-Valley Locking Spin Valve. *Phys. Rev. B* **2019**, *100* (16), 161110.
- (11) Xu, X.; Yao, W.; Xiao, D.; Heinz, T. F. Spin and Pseudospins in Layered Transition Metal Dichalcogenides. *Nature Phys* **2014**, *10* (5), 343–350.
- (12) Li, Y.; Ludwig, J.; Low, T.; Chernikov, A.; Cui, X.; Arefe, G.; Kim, Y. D.; Van Der Zande, A. M.; Rigosi, A.; Hill, H. M.; Kim, S. H.; Hone, J.; Li, Z.; Smirnov, D.; Heinz, T. F. Valley Splitting and Polarization by the Zeeman Effect in Monolayer MoSe₂. *Phys. Rev. Lett.* **2014**, *113* (26), 266804.

- (13) MacNeill, D.; Heikes, C.; Mak, K. F.; Anderson, Z.; Kormányos, A.; Zólyomi, V.; Park, J.; Ralph, D. C. Breaking of Valley Degeneracy by Magnetic Field in Monolayer MoSe₂. *Phys. Rev. Lett.* **2015**, *114* (3), 037401.
- (14) Aivazian, G.; Gong, Z.; Jones, A. M.; Chu, R.-L.; Yan, J.; Mandrus, D. G.; Zhang, C.; Cobden, D.; Yao, W.; Xu, X. Magnetic Control of Valley Pseudospin in Monolayer WSe₂. *Nature Phys* **2015**, *11* (2), 148–152.
- (15) Srivastava, A.; Sidler, M.; Allain, A. V.; Lembke, D. S.; Kis, A.; Imamoglu, A. Valley Zeeman Effect in Elementary Optical Excitations of Monolayer WSe₂. *Nature Phys* **2015**, *11* (2), 141–147.
- (16) Peng, R.; Ma, Y.; Zhang, S.; Huang, B.; Dai, Y. Valley Polarization in Janus Single-Layer MoSSe via Magnetic Doping. *J. Phys. Chem. Lett.* **2018**, *9* (13), 3612–3617.
- (17) Zhou, J.; Lin, J.; Sims, H.; Jiang, C.; Cong, C.; Brehm, J. A.; Zhang, Z.; Niu, L.; Chen, Y.; Zhou, Y.; Wang, Y.; Liu, F.; Zhu, C.; Yu, T.; Suenaga, K.; Mishra, R.; Pantelides, S. T.; Zhu, Z.; Gao, W.; Liu, Z.; Zhou, W. Synthesis of Co-Doped MoS₂ Monolayers with Enhanced Valley Splitting. *Adv. Mater.* **2020**, *32* (11), 1906536.
- (18) Matsuoka, H.; Habe, T.; Iwasa, Y.; Koshino, M.; Nakano, M. Spontaneous Spin-Valley Polarization in NbSe₂ at a van Der Waals Interface. *Nat Commun* **2022**, *13* (1), 5129.
- (19) Zhong, D.; Seyler, K. L.; Linpeng, X.; Wilson, N. P.; Taniguchi, T.; Watanabe, K.; McGuire, M. A.; Fu, K.-M. C.; Xiao, D.; Yao, W.; Xu, X. Layer-Resolved Magnetic Proximity Effect in van Der Waals Heterostructures. *Nat. Nanotechnol.* **2020**, *15* (3), 187–191.
- (20) Abdollahi, M.; Tagani, M. B. Tuning the Magnetic Properties of a VSe₂ Monolayer via the Magnetic Proximity Effect Mediated by Zeeman-Type Spin-Orbit Interaction. *Phys. Rev. B* **2023**, *108* (2), 024427.
- (21) Zhang, W.; Zhu, H.; Zhang, W.; Wang, J.; Zhang, T.; Yang, S.; Shao, B.; Zuo, X. Manipulation of Valley-Pseudospin in 2D WTe₂/CrI₃ van Der Waals Heterostructure by Magnetic Proximity Effect. *Applied Surface Science* **2024**, *647*, 158986.
- (22) Mak, K. F.; He, K.; Shan, J.; Heinz, T. F. Control of Valley Polarization in Monolayer MoS₂ by Optical Helicity. *Nature Nanotech* **2012**, *7* (8), 494–498.
- (23) Hsu, W.-T. Optically Initialized Robust Valley-Polarized Holes in Monolayer WSe₂. *NATURE COMMUNICATIONS* **2015**.
- (24) Xie, W.; Zhang, L.; Yue, Y.; Li, M.; Wang, H. Giant Valley Polarization and Perpendicular Magnetocrystalline Anisotropy Energy in Monolayer MX₂ (M = Ru, Os; X = Cl, Br). *Phys. Rev. B* **2024**, *109* (2), 024406.
- (25) Pan, W. Tuning the Magnetic Anisotropy and Topological Phase with Electronic Correlation in Single-Layer H-FeBr₂. *Phys. Rev. B* **2022**, *106* (12), 125122.
- (26) Zhao, J.; Zhang, T.; Peng, R.; Dai, Y.; Huang, B.; Ma, Y. Spontaneous Valley Polarization and Electrical Control of Valley Physics in Single-Layer TcIrGe₂S₆. *J. Phys. Chem. Lett.* **2022**, *13* (37), 8749–8754.
- (27) Dai, Y.; Feng, X.; Xu, X.; He, Z.; Peng, R.; Huang, B.; Ma, Y. Valley-Related Multiple Hall Effect in Monolayer VSi₂P₄. *Phys. Rev. B* **2021**, *104* (7), 075421.
- (28) Zhao, P.; Ma, Y.; Lei, C.; Wang, H.; Huang, B.; Dai, Y. Single-Layer LaBr₂: Two-Dimensional Valleytronic Semiconductor with Spontaneous Spin and Valley Polarizations. *Appl. Phys. Lett.* **2019**, *115* (26), 261605.
- (29) Sheng, K.; Zhang, B.; Yuan, H.-K.; Wang, Z.-Y. Strain-Engineered Topological Phase

- Transitions in Ferrovalley 2 H–RuCl₂ Monolayer. *Phys. Rev. B* **2022**, *105* (19), 195312.
- (30) Cheng, H.-X.; Zhou, J.; Ji, W.; Zhang, Y.-N.; Feng, Y.-P. Two-Dimensional Intrinsic Ferrovalley GdI₂ with Large Valley Polarization. *Phys. Rev. B* **2021**, *103* (12), 125121.
- (31) Liu, Y.; Feng, Y.; Zhang, T.; He, Z.; Dai, Y.; Huang, B.; Ma, Y. Strain-Valley Coupling in 2D Antiferromagnetic Lattice. *Adv Funct Materials* **2023**, 2305130.
- (32) Zhang, D.; Li, A.; Chen, X.; Zhou, W.; Ouyang, F. Tuning Valley Splitting and Magnetic Anisotropy of Multiferroic CuMP₂X₆ (M = Cr, V; X = S, Se) Monolayer. *Phys. Rev. B* **2022**, *105* (8), 085408.
- (33) Šmejkal, L.; Sinova, J.; Jungwirth, T. Beyond Conventional Ferromagnetism and Antiferromagnetism: A Phase with Nonrelativistic Spin and Crystal Rotation Symmetry. *Phys. Rev. X* **2022**, *12* (3), 031042.
- (34) Šmejkal, L.; Sinova, J.; Jungwirth, T. Emerging Research Landscape of Altermagnetism. *Phys. Rev. X* **2022**, *12* (4), 040501.
- (35) Šmejkal, L.; González-Hernández, R.; Jungwirth, T.; Sinova, J. Crystal Time-Reversal Symmetry Breaking and Spontaneous Hall Effect in Collinear Antiferromagnets. *Sci. Adv.* **2020**, *6* (23), eaaz8809.
- (36) Leeb, V.; Mook, A.; Šmejkal, L.; Knolle, J. Spontaneous Formation of Altermagnetism from Orbital Ordering. *Phys. Rev. Lett.* **2024**, *132* (23), 236701.
- (37) Reimers, S.; Odenbreit, L.; Šmejkal, L.; Strocov, V. N.; Constantinou, P.; Hellenes, A. B.; Jaeschke Ubierno, R.; Campos, W. H.; Bharadwaj, V. K.; Chakraborty, A.; Denneulin, T.; Shi, W.; Dunin-Borkowski, R. E.; Das, S.; Kläui, M.; Sinova, J.; Jourdan, M. Direct Observation of Altermagnetic Band Splitting in CrSb Thin Films. *Nat Commun* **2024**, *15* (1), 2116.
- (38) Wu, Y.; Deng, L.; Yin, X.; Tong, J.; Tian, F.; Zhang, X. Valley-Related Multipiezo Effect and Noncollinear Spin Current in an Altermagnet Fe₂Se₂O Monolayer. *Nano Lett.* **2024**, acs.nanolett.4c02554.
- (39) Zhu, Y.; Chen, T.; Li, Y.; Qiao, L.; Ma, X.; Liu, C.; Hu, T.; Gao, H.; Ren, W. Multipiezo Effect in Altermagnetic V₂SeTeO Monolayer. *Nano Lett.* **2024**, *24* (1), 472–478.
- (40) Ma, H.-Y.; Hu, M.; Li, N.; Liu, J.; Yao, W.; Jia, J.-F.; Liu, J. Multifunctional Antiferromagnetic Materials with Giant Piezomagnetism and Noncollinear Spin Current. *Nat Commun* **2021**, *12* (1), 2846.
- (41) Guo, S.-D.; Guo, X.-S.; Cheng, K.; Wang, K.; Ang, Y. S. Piezoelectric Altermagnetism and Spin-Valley Polarization in Janus Monolayer Cr₂SO. *Applied Physics Letters* **2023**, *123* (8), 082401.
- (42) Chen, X.; Wang, D.; Li, L.; Sanyal, B. Giant Spin-Splitting and Tunable Spin-Momentum Locked Transport in Room Temperature Collinear Antiferromagnetic Semimetallic CrO Monolayer. *Applied Physics Letters* **2023**, *123* (2), 022402.
- (43) Mermin, N. D.; Wagner, H. Absence of Ferromagnetism or Antiferromagnetism in One- or Two-Dimensional Isotropic Heisenberg Models. *Phys. Rev. Lett.* **1966**, *17* (22), 1133–1136.
- (44) Ma, Y.; Wu, Y.; Tong, J.; Deng, L.; Yin, X.; Zhou, L.; Han, X.; Tian, F.; Zhang, X. Distinct Ferrovalley Characteristics of the Janus RuCl_X (X = F, Br) Monolayer. *Nanoscale* **2023**, *15* (18), 8278–8288.
- (45) Wu, Y.; Tong, J.; Deng, L.; Luo, F.; Tian, F.; Qin, G.; Zhang, X. Realizing Spontaneous Valley Polarization and Topological Phase Transitions in Monolayer ScX₂ (X = Cl, Br, I).

Acta Materialia **2023**, *246*, 118731.

- (46) Cui, Q.; Zhu, Y.; Liang, J.; Cui, P.; Yang, H. Spin-Valley Coupling in a Two-Dimensional VSi_2N_4 Monolayer. *Phys. Rev. B* **2021**, *103* (8), 085421.
- (47) Blöchl, P. E. Projector Augmented-Wave Method. *Phys. Rev. B* **1994**, *50* (24), 17953–17979.
- (48) Kresse, G.; Furthmüller, J. Efficiency of Ab-Initio Total Energy Calculations for Metals and Semiconductors Using a Plane-Wave Basis Set. *Computational Materials Science* **1996**, *6* (1), 15–50.
- (49) Perdew, J. P.; Burke, K.; Ernzerhof, M. Generalized Gradient Approximation Made Simple. *Phys. Rev. Lett.* **1996**, *77* (18), 3865–3868.
- (50) Weinert, M.; Watson, R. E.; Davenport, J. W. Total-Energy Differences and Eigenvalue Sums. *Phys. Rev. B* **1985**, *32* (4), 2115–2119.
- (51) Daalderop, G. H. O.; Kelly, P. J.; Schuurmans, M. F. H. First-Principles Calculation of the Magnetocrystalline Anisotropy Energy of Iron, Cobalt, and Nickel. *Phys. Rev. B* **1990**, *41* (17), 11919–11937.
- (52) Togo, A.; Tanaka, I. First Principles Phonon Calculations in Materials Science. *Scripta Materialia* **2015**, *108*, 1–5.
- (53) Nosé, S. A Unified Formulation of the Constant Temperature Molecular Dynamics Methods. *The Journal of Chemical Physics* **1984**, *81* (1), 511–519.
- (54) Evans, R. F. L.; Fan, W. J.; Chureemart, P.; Ostler, T. A.; Ellis, M. O. A.; Chantrell, R. W. Atomistic Spin Model Simulations of Magnetic Nanomaterials. *J. Phys.: Condens. Matter* **2014**, *26* (10), 103202.
- (55) Evans, R. F. L.; Atxitia, U.; Chantrell, R. W. Quantitative Simulation of Temperature-Dependent Magnetization Dynamics and Equilibrium Properties of Elemental Ferromagnets. *Phys. Rev. B* **2015**, *91* (14), 144425.
- (56) Liu, G.-B.; Shan, W.-Y.; Yao, Y.; Yao, W.; Xiao, D. Three-Band Tight-Binding Model for Monolayers of Group-VIB Transition Metal Dichalcogenides. *Phys. Rev. B* **2013**, *88* (8), 085433.
- (57) He, X.; Helbig, N.; Verstraete, M. J.; Bousquet, E. TB2J: A Python Package for Computing Magnetic Interaction Parameters. *Computer Physics Communications* **2021**, *264*, 107938.
- (58) Zhang, C.; Nie, Y.; Sanvito, S.; Du, A. First-Principles Prediction of a Room-Temperature Ferromagnetic Janus VSSe Monolayer with Piezoelectricity, Ferroelasticity, and Large Valley Polarization. *Nano Lett.* **2019**, *19* (2), 1366–1370.
- (59) Dai, Y.; Zang, Y.; Ma, Y.; Peng, R.; Wang, H.; Huang, B. Large Valley-Polarized State in Single-Layer NbX_2 ($X = \text{S}, \text{Se}$): Theoretical Prediction. *Nano Res.* **2021**, *14* (3), 834–839.
- (60) Du, W.; Ma, Y.; Peng, R.; Wang, H.; Huang, B.; Dai, Y. Prediction of Single-Layer TiVI_6 as a Promising Two-Dimensional Valleytronic Semiconductor with Spontaneous Valley Polarization. *J. Mater. Chem. C* **2020**, *8* (38), 13220–13225.
- (61) Zhao, P.; Ma, Y.; Lei, C.; Wang, H.; Huang, B.; Dai, Y. Single-Layer LaBr_2 : Two-Dimensional Valleytronic Semiconductor with Spontaneous Spin and Valley Polarizations. *Applied Physics Letters* **2019**, *115* (26), 261605.